

Retinal Vessel Segmentation with Deep Graph and Capsule Reasoning

Xinxu Wei^{a,c}, Xi Lin^c, Shixuan Zhao^c, Haiyun Liu^b, Yongjie Li^{*a,c}

^a*Yangtze Delta Region Institute (Huzhou), University of Electronic Science and Technology of China, Chengdu, China*

^b*Department of Computer Science and Engineering, University of South Florida, Tampa, FL, USA*

^c*School of Life Science and Technology, University of Electronic Science and Technology of China, Chengdu, China*

Abstract

Effective retinal vessel segmentation requires a sophisticated integration of global contextual awareness and local vessel continuity. To address this challenge, we propose the Graph Capsule Convolution Network (GCC-UNet), which merges capsule convolutions with CNNs to capture both local and global features. The Graph Capsule Convolution operator is specifically designed to enhance the representation of global context, while the Selective Graph Attention Fusion module ensures seamless integration of local and global information. To further improve vessel continuity, we introduce the Bottleneck Graph Attention module, which incorporates Channel-wise and Spatial Graph Attention mechanisms. The Multi-Scale Graph Fusion module adeptly combines features from various scales. Our approach has been rig-

*This work was supported by Huzhou Science and Technology Program (#2023GZ13).

*Corresponding author

Email addresses: xxwei523@gmail.com (Xinxu Wei), xi.lin@std.uestc.edu.cn (Xi Lin), phanzsx@gmail.com (Shixuan Zhao), 1335914484@qq.com (Haiyun Liu), liyj@uestc.edu.cn (Yongjie Li*)

orously validated through experiments on widely used public datasets, with ablation studies confirming the efficacy of each component. Comparative results highlight GCC-UNet’s superior performance over existing methods, setting a new benchmark in retinal vessel segmentation. Notably, this work represents the first integration of vanilla, graph, and capsule convolutional techniques in the domain of medical image segmentation.

Keywords: Retinal vessel segmentation, Deep learning, Graph convolution, Capsule convolution

1. Introduction

Retinal vessel segmentation is a key step in diagnosing retinal diseases like diabetic retinopathy and glaucoma, as changes in the vascular structure offer important diagnostic insights [1]. However, manually segmenting vessels is often labor-intensive and prone to mistakes, especially when addressing thin, low-contrast vessels against the intricate background of the fundus. Therefore, developing automated and accurate segmentation algorithms is critical for improving clinical workflow.

The segmentation task is challenging due to the intricate structure of retinal vessels, which often blend into the background or are obscured by lesions. Thin vessels, especially capillaries, are hard to detect and frequently mislabeled due to their similar characteristics to the surrounding tissues [2, 3]. Although traditional methods [4][5] and machine learning-based techniques have shown some success [6], they often rely on pre-defined features and struggle with the fine details necessary for accurate segmentation.

Recently, deep learning techniques have become dominant in the field,

achieving cutting-edge performance in medical image segmentation [7][8]. Despite these advances, two key challenges remain: capturing comprehensive global context and ensuring vessel continuity, particularly for the smallest vessels. Methods such as dilated convolutions [9], attention mechanisms [10], and non-local operations [11] have been proposed to address these issues. However, these methods often fail to fully model the part-to-whole relationships essential for context in retinal images, while existing loss functions and attention modules struggle to maintain vessel continuity amidst noise from other tissues or lesions. To tackle these challenges, we propose a Graph Capsule Convolution UNet (GCC-UNet), which introduces capsule convolutions for part-to-whole modeling and graph reasoning to enhance vessel continuity. This framework uniquely combines vanilla convolution, capsule convolution, and graph convolution, leveraging their complementary strengths to achieve more robust segmentation.

The main contributions of this work are:

- We present the GCC-UNet, which captures both local features and global contextual information for retinal vessel segmentation.
- We introduce the Graph Capsule Convolution (GC-Conv) operator, integrating graph reasoning into capsule networks to improve the representation of global vessel structures.
- We develop the Selective Graph Attention Fusion (SGAF) module, designed to effectively merge global and local context features.
- We propose a Bottleneck Graph Attention (BGA) module, which improves vessel continuity through Channel-wise and Spatial Graph At-

tention mechanisms.

- We design a Multi-Scale Graph Fusion (MSGF) module that combines features at different scales to enhance segmentation performance.
- Extensive experiments on various datasets demonstrate that our approach surpasses existing methods, setting a new benchmark in retinal vessel segmentation.

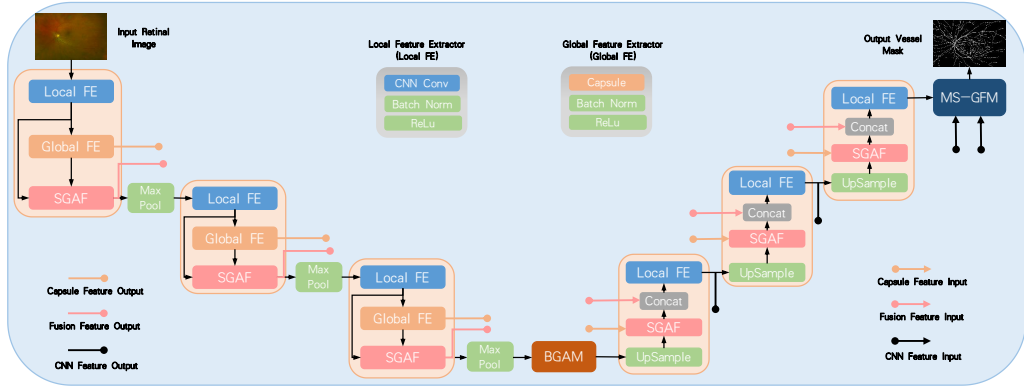


Figure 1: The network architecture of the proposed GCC-UNet.

2. Related Works

Traditional approaches utilize a variety of image processing techniques, such as filtering [5, 12] and handcrafted feature extraction [4, 12], to distinguish retinal vessels from the background. Numerous studies have explored vessel attributes like orientation [13], edge detection [14], line patterns [15, 16], vessel width [17], and structural topology [18], contributing to improved segmentation. Furthermore, machine learning-based approaches

[19, 20, 18], including classifiers such as Support Vector Machines (SVMs) [15], have demonstrated efficacy in vessel segmentation tasks.

In recent years, deep learning techniques [21, 22, 23] have gained prominence due to their robust feature extraction capabilities. For instance, DeepVessel [24] adopts a HED-like architecture combined with Conditional Random Fields (CRFs) for vessel detection. Other deep learning approaches, such as DRIU [25], VGN [26], V-GAN [27], BTS-DSN [28], SWT-FCN [29], DeepDyn [30], and DRIS-GP [31], have achieved noteworthy results. UNet [32], a well-established model in medical image segmentation, has inspired various UNet-based models for retinal vessel segmentation, including Attention UNet [33], Dense UNet [34], Deformable UNet [35], SA-UNet [36], JL-UNet [37], CC-Net [8], CTF-Net [38], CSU-Net [7], OCE-Net [39] and RCAR-UNet [40].

Despite these advancements, many methods struggle to fully capture the intricate relationships between vessel characteristics and ensure vessel continuity, especially when external noise is present.

2.1. Graph Neural Networks

Graph neural networks (GNNs), particularly graph convolutional networks (GCNs) [41, 42], have garnered considerable attention across diverse fields such as computer vision [43, 44]. Initially proposed by Kipf [42] for the classification of non-Euclidean data, GCNs have since been employed in tasks including image recognition [44], segmentation [43], and medical image analysis [45]. Despite the significant advancements in GNN research [46, 47], their application in vessel segmentation remains relatively underexplored [26].

Our research addresses this gap by incorporating a GCN module specifi-

cally designed for retinal vessel segmentation, leveraging the geometric modeling capabilities of GCNs. By capturing the structural features of vessels, we aim to enhance vessel continuity and minimize interference from surrounding tissues.

2.2. Capsule Neural Networks

Capsule networks, which are specifically designed to capture spatial relationships between objects, excel in distinguishing multiple overlapping entities within an image. Hinton [48] introduced the concept of capsules to address the limitations of CNNs, particularly their restricted ability to capture global context due to limited receptive fields and their lack of equivariance. Sabour’s [48] capsule network architecture employs dynamic routing between capsule units to represent part-whole relationships, thereby enhancing equivariance. Since this introduction, several enhancements such as Attentive Capsule Networks [49], Graph-Capsule Networks [50, 51], and DeformCaps [52], along with innovations in routing mechanisms (e.g., EM-Routing [53] and Self-Attention Routing [54]), have broadened the applicability of capsule networks in tasks such as object detection, image classification, and medical image segmentation [55, 56].

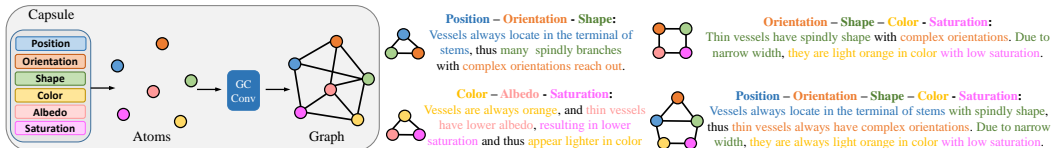
However, most capsule-based methods focus on optimizing routing algorithms rather than addressing the relationships between capsule elements. Inspired by retinal vessel characteristics, we introduce capsule networks to retinal vessel segmentation, employing their global context modeling capabilities. By incorporating graph reasoning into capsule networks, our approach captures interactions between capsule elements, enhancing vessel continuity while maintaining context awareness.

3. Methodology

3.1. Overall Architecture

The GCC-UNet architecture, illustrated in Figure 1, builds upon the U-Net [32] as its foundational framework. In the downsampling process, a Local Feature Extractor (Local FE), a Global Feature Extractor (Global FE), and a Selective Graph Attention Fusion (SGAF) module are introduced to combine local features captured by a conventional CNN with global context features derived from a Capsule Neural Network. To achieve global feature extraction, we propose a Graph Capsule Convolution (GC Conv) operator, which replaces the standard capsule convolution operator. Additionally, a Bottleneck Graph Attention (BGA) module is integrated into the bottleneck to enhance vessel continuity by modeling the connectivity of vessel nodes along the graph. In the upsampling phase, the global context features are directly passed to the upsampling layer, minimizing computational overhead. The SGAF then fuses the global features with the upsampled local features. Lastly, a Multi-Scale Graph Fusion (MSGF) module is employed to integrate features across different stages of the U-Net.

3.2. Graph Capsule Convolution



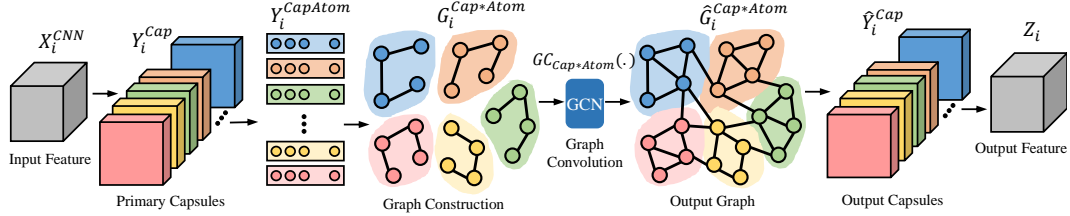


Figure 3: The proposed Graph Capsule Convolution (GC Conv).

Unlike traditional CNNs that utilize scalar elements, capsule networks (CapsNets) employ vectors as their fundamental components. Each capsule contains a vector that captures various intrinsic characteristics of an object, such as its pose (position, size, orientation, shape), deformation, color, and saturation. The length of the vector represents the probability of the object’s presence in the image. While CapsNets excel in capturing detailed local features, they struggle with modeling translation invariance and part-to-whole relationships compared to CNNs.

To improve global feature extraction for retinal vessels, we enhance the standard capsule convolution [48] by integrating graph representation learning to model the relationships among capsules. We propose a novel Graph Capsule Convolution (GC Conv).

As illustrated in Fig. 3, the input features extracted by a conventional CNN are transformed into primary capsules, representing low-level entities. Dynamic routing [48] then directs these low-level capsules to high-level ones, capturing part-to-whole relationships. This dynamic routing operates as a transfer matrix with attention weights, emphasizing important capsules and vectors while disregarding less relevant ones. However, the original dynamic routing [48] does not account for correlations among different capsules and

atoms within capsules. To address this, we incorporate graph reasoning into the dynamic routing process, as shown in Fig. 3, to better model these correlations. This approach enables us to effectively capture relationships among channels, capsules, and atoms.

As shown in Fig. 3, the input CNN feature X_i^{CNN} with a shape of $[B, C, H, W]$ is transformed into the primary capsules Y_i^{Cap} , which have a shape of $[B, H, W, k^2, C, L, V]$, where B , H , W , C , L , and V represent the numbers of batch sizes, height, width, channels, capsules, and atoms in each capsule, respectively.

$$X_i^{CNN} \xrightarrow{\text{Transform}} Y_i^{Cap} \quad (1)$$

And the channel dimension of Y_i^{Cap} is split from the features to obtain independent features $Y_i^{Channel}$ with a shape of $[B, H, W, k^2, C, 1, 1]$, which are independent of the dimensions of capsules and atoms. Similarly, the dimensions of capsules and atoms are split to obtain independent features $Y_i^{CapAtom}$ with a shape of $[B, H, W, k^2, 1, L, V]$. By multiplying the channels of capsules and atoms dimensions, we obtain the feature of $Y_i^{Cap*Atom}$ with a shape of $[B, H, W, k^2, 1, L * V]$.

$$Y_i^{Cap} \xrightarrow[\text{Channel-wise}]{\text{Split}} Y_i^{Channel}, \quad Y_i^{CapAtom} \quad (2)$$

We then use average pooling to remove the H , W , and K^2 dimensions and construct a graph $G_i^{Channel}$ along the channel dimension C for $Y_i^{Channel}$.

$$\begin{aligned} Y_i^{Channel} &\xrightarrow[\text{Channel-wise}]{\text{GraphConstruction}} G_i^{Channel} \\ Y_i^{Cap*Atom} &\xrightarrow[\text{Channel-wise}]{\text{GraphConstruction}} G_i^{Cap*Atom} \end{aligned} \quad (3)$$

Similarly, we construct a graph $G_i^{Cap*Atom}$ along the $L * V$ dimension for $Y_i^{Cap*Atom}$. We apply a graph convolution $GC_{Channel}(.)$ on $G_i^{Channel}$ to obtain the output graph feature $\widehat{G}_i^{Channel}$. We also apply a graph convolution $GC_{Cap*Atom}(.)$ on $G_i^{Cap*Atom}$ to obtain the output graph feature $\widehat{G}_i^{Cap*Atom}$.

$$\begin{aligned}\widehat{G}_i^{Channel} &= GC_{Channel}(G_i^{Channel}) \\ \widehat{G}_i^{Cap*Atom} &= GC_{Cap*Atom}(G_i^{Cap*Atom})\end{aligned}\tag{4}$$

Finally, we integrate $\widehat{G}_i^{Channel}$ and $\widehat{G}_i^{Cap*Atom}$ using addition and expansion operators, and transfer them into capsule features \widehat{Y}_i^{Cap} to obtain the output feature Z_i .

3.3. Selective Graph Attention Fusion Module

Incorporating global context is essential for models to handle variations in scale, orientation, and partial occlusions of fundus vessels. However, capsule neural networks (CapsNets) face challenges in learning crucial local features. To address this, a promising approach is to combine capsule convolution with traditional CNN models, enabling the model to capture both local and global features effectively.

To achieve optimal fusion performance, we propose a novel Selective Graph Attention Fusion (SGAF) module. This module leverages the graph structure to model the relationships within channels of both local and global features, while also learning the correlations between these features.

In Fig. 4, we have two types of input features: local features X_i^{Local} obtained through plain CNN convolution, and global context features X_i^{Global} obtained through capsule convolution. Then we add X_i^{Local} and X_i^{Global} to obtain the fused feature X_i^{Fusion} . We then apply three independent Average Pooling operators to eliminate spatial dimensions, preserving only the

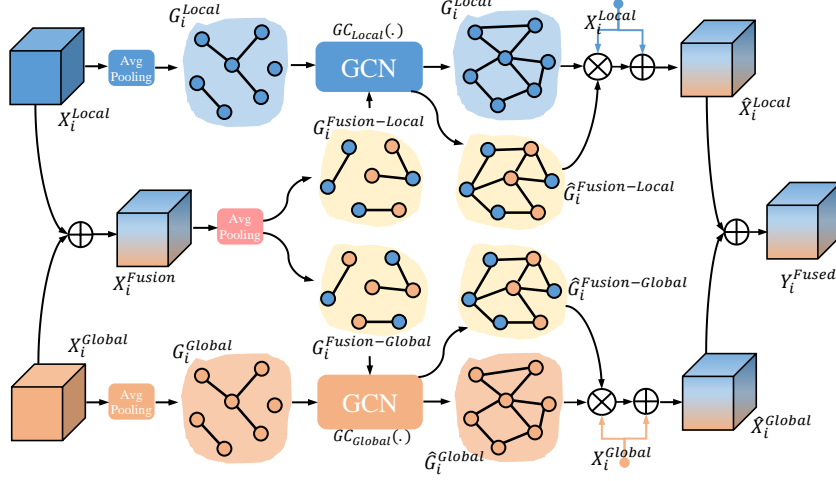


Figure 4: The architecture of the proposed Selective Graph Attention Fusion (SGAF) module.

channel dimension. After pooling, we construct graphs along the channel dimension of the three features, resulting in four independent graphs: G_i^{Local} , G_i^{Global} , $G_i^{Fusion-Local}$ and $G_i^{Fusion-Global}$. The two graphs $G_i^{Fusion-Local}$ and $G_i^{Fusion-Global}$ constructed from X_i^{Fusion} provide shared fusion information for both the local feature X_i^{Local} and global feature X_i^{Global} . We assume that the two graphs should contain different topological structures of channels from X_i^{Local} and X_i^{Global} after learning and reweighting the graph convolution operators.

$$\begin{aligned} G_i^\alpha &= \text{AvgPooling}(X_i^\alpha) \quad (\alpha \in [\text{Global}, \text{Local}]) \\ \hat{G}_i^\alpha &= GC_\alpha(G_i^\alpha) \quad (\alpha \in [\text{Global}, \text{Local}]) \end{aligned} \tag{5}$$

The graph represents each channel of the feature as a node. To learn the connectivity and relationships among nodes (channels), we apply only two graph convolution operators on the four constructed graphs: $GC_{Local}(\cdot)$ for G_i^{Local} and $G_i^{Fusion-Local}$, and $GC_{Global}(\cdot)$ for G_i^{Global} and $G_i^{Fusion-Global}$. By using shared graph convolution, the local or global graphs can share nodes

and connectivity information with the fusion graphs, resulting in better connectivity weight adjustment, allowing more informative representation flow on the graph, and reducing computational cost and parameters.

$$\begin{aligned} G_i^{Fusion-\alpha} &= \text{Split}(\text{AvgPooling}(X_i^{Fusion-\alpha})) \\ \widehat{G}_i^{Fusion-\alpha} &= GC_\alpha(G_i^{Fusion-\alpha}) \quad (\alpha \in [Global, Local]) \end{aligned} \quad (6)$$

After applying graph convolution, we obtain four output graphs: \widehat{G}_i^{Local} , $\widehat{G}_i^{Fusion-Local}$, \widehat{G}_i^{Global} , and $\widehat{G}_i^{Fusion-Global}$. We then apply \widehat{G}_i^{Local} and \widehat{G}_i^{Global} on the input features X_i^{Local} and X_i^{Global} using multiplication and addition operators, respectively, which can be viewed as a kind of self-attention because the graph attention weights generated from the input features are applied back on the channels of original input features. At the same time, $\widehat{G}_i^{Fusion-Local}$ and $\widehat{G}_i^{Fusion-Global}$ are applied on the input features X_i^{Local} and X_i^{Global} using multiplication operators. The resulted refined output features are denoted as \widehat{X}_i^{Local} and \widehat{X}_i^{Global} .

$$\begin{aligned} \widehat{X}_i^\alpha &= X_i^\alpha * \text{Expand}(\widehat{G}_i^\alpha * \widehat{G}_i^{Fusion-\alpha}) + X_i^\alpha \\ (\alpha &\in [Global, Local]) \end{aligned} \quad (7)$$

Finally, we add \widehat{X}_i^{Local} and \widehat{X}_i^{Global} together to obtain the fused feature Y_i^{Fused} .

$$Y_i^{Fused} = \widehat{X}_i^{Local} + \widehat{X}_i^{Global} \quad (8)$$

3.4. Bottleneck Graph Attention Module

To improve vessel continuity, particularly for thin vessels, we propose a novel Bottleneck Graph Attention (BGA) module comprising of Channel-wise Graph Attention (CGA) and Spatial Graph Attention (SGA). The input features X_i are first fed into CGA, where an Average Pooling operator

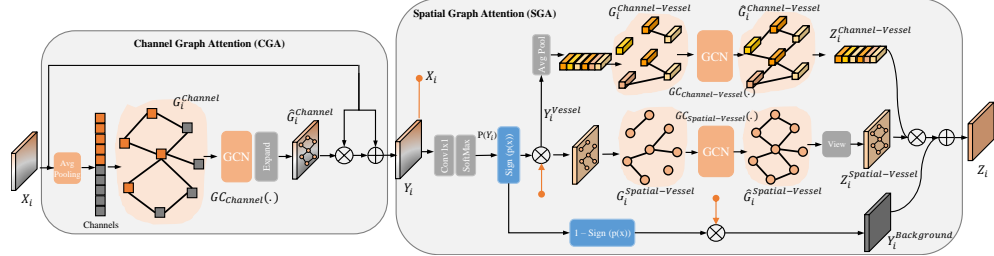


Figure 5: The architecture of the proposed Bottleneck Graph Attention (BGA) module.

is used to extract channel-only features, transforming the feature shape from $[B, C, H, W]$ to $[B, C, 1, 1]$. A graph $G_i^{Channel}$ is constructed along the channel dimension, where each node represents a channel of features and the edge connectivity between nodes indicates their relationship. A graph convolution operator $GC_{Channel}(\cdot)$ is applied to $G_i^{Channel}$, producing an output graph $\widehat{G}_i^{Channel}$ with re-weighted connectivity and re-modelled channel relationships. The refined graph $\widehat{G}_i^{Channel}$ is then expanded along the spatial dimensions and recovered to $[B, C, H, W]$.

$$\widehat{G}_i^{Channel} = GC_{Channel}(AvgPooling(X_i)) \quad (9)$$

The refined feature and graph representation $\widehat{G}_i^{Channel}$ are fused with the input feature X_i through multiplication and addition, generating the output feature Y_i . The CGA module enables the representation of channel dependencies as a graph and captures the relationships among channels.

$$Y_i = X_i * Expand(\widehat{G}_i^{Channel}) + X_i \quad (10)$$

In the SGA module, the input feature is Y_i , and a feature selector is proposed to extract vessels from the fundus background. The feature selector applies a conv1x1 $Conv(\cdot)$ operator to reduce the dimension of Y_i and Softmax function

$\text{Softmax}(.)$ to calculate a probability map $p(Y_i)$, which contains information about the probability that each pixel belongs to a vessel, ranging from 0 to 1.

$$p(Y_i) = \text{Softmax}(\text{Conv}(Y_i)) \quad (11)$$

A pre-defined piecewise function called the Sign function called the Sign function $\text{Sign}(.)$ is then applied to separate the probability values into two intervals. Specifically, a threshold of 0.4 was set in our experiments, indicating that the pixels with probability values greater than 0.4 correspond to blood vessel pixels, while those with values less than 0.4 correspond to background pixels. This allows for effective separation of vessel regions from the background. The $\text{Sign}(.)$ function is defined as

$$\text{Sign}(x) = \begin{cases} 1 & x > 0.4 \quad (\text{Vessel}) \\ 0 & x < 0.4 \quad (\text{Background}) \end{cases} \quad (12)$$

where x means the probability of each pixel in the probability map $p(Y_i)$. Using the Sign function, we can obtain vessel features Y_i^{Vessel} and background features $Y_i^{\text{Background}}$ separately from input features Y_i based on their probability values.

$$Y_i^{\text{Vessel}}, \quad Y_i^{\text{Background}} = \text{Sign}(Y_i) \quad (13)$$

To improve the continuity of vessels, we perform two individual operations. The first operation involves constructing a graph $G_i^{\text{Spatial-Vessel}}$ for the vessel-only features based on their spatial distribution. Nodes and edges in the graph represent the vessels and their connectivity, respectively. We then apply a graph convolution $GC_{\text{Spatial-Vessel}}(.)$ on the graph $G_i^{\text{Spatial-Vessel}}$ to

learn information about the nodes and edges connectivity, aiming to improve the continuity of vessels without interference from the background, especially noise and other tissues in the background. This yields the output features of vessels $Z_i^{Spatial-Vessel}$.

$$Z_i^{Spatial-Vessel} = GC_{Spatial-Vessel}(G_i^{Spatial-Vessel}) \quad (14)$$

In addition to improving vascular continuity in spatial distribution, we also enhance semantic consistency. To achieve this, we use an average pooling operator to extract channel information of vessels, and construct a graph $G_i^{Channel-Vessel}$ for these channels. We then apply a graph convolution operator $GC_{Channel-Vessel}(.)$ to learn the graph representation of channels, yielding the output features of vessels $Z_i^{Channel-Vessel}$.

$$Z_i^{Channel-Vessel} = GC_{Channel-Vessel}(G_i^{Channel-Vessel}) \quad (15)$$

Finally, we multiply $Z_i^{Spatial-Vessel}$ and $Z_i^{Channel-Vessel}$, add $Y_j^{Background}$, and then obtain the refined features Z_i whose vascular continuity has been enhanced.

$$Z_i = Z_i^{Channel-Vessel} * Z_i^{Spatial-Vessel} + Y_j^{Background} \quad (16)$$

Through this approach, we can improve the connectivity of vessels without being affected by other tissues.

3.5. Multi-Scale Graph Fusion Module

To integrate the multi-scale features extracted from different stages of the UNet, we propose a Multi-Scale Graph Fusion module, as shown in Fig. 6. The input features X_i^a , X_i^b and X_i^c are obtained from different upsampling stages of the UNet. Firstly, we apply upsampling and conv1x1 operators on

X_i^b and X_i^c to reshape their spatial and channel dimensions to match those of X_i^a .

$$G_i^\alpha = \text{AvgPooling}(\text{Up}(\text{Conv1x1}(X_i^\alpha))) \quad (\alpha \in [b, c]) \quad (17)$$

Subsequently, we apply Average Pooling operators on these features to reduce their dimensions and preserve only channel-wise information. Then, we construct three independent graphs, G_i^a , G_i^b and G_i^c , for these features along the channel-wise dimension.

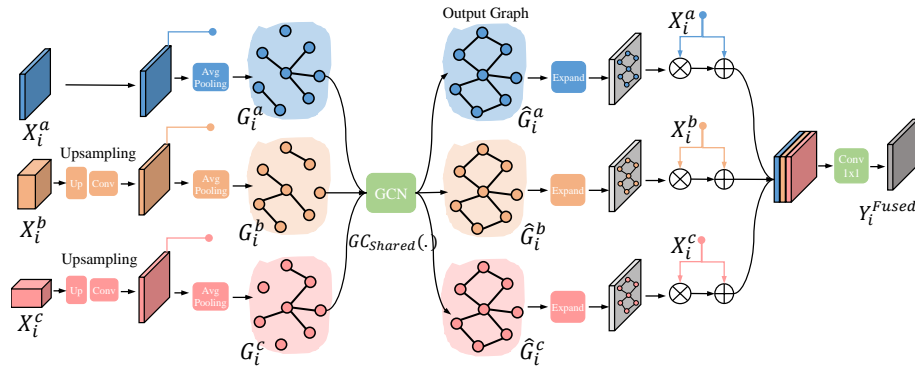


Figure 6: The proposed Multi-Scale Graph Fusion (MSGF) module.

Instead of adopting three individual graph convolution on these three independent graphs, we use only a single shared graph convolution $GC_{Shared}(\cdot)$ to conduct convolutional process on G_i^a , G_i^b and G_i^c , because we assume that graphs constructed from different scales with the same input feature have similar graph patterns and node connectivities. Adopting shared graph convolution can simultaneously capture the topological structure representations of G_i^a , G_i^b and G_i^c , and adjust the connectivity of nodes on the graph by taking other graphs into the consideration, so that the information can propagate and flow on the graphs constructed from multi-scale features. After applying

graph convolution operators, we obtain three independent graph representations \widehat{G}_i^a , \widehat{G}_i^b and \widehat{G}_i^c .

$$\widehat{G}_i^\alpha = GC_{Shared}(G_i^\alpha) \quad (\alpha \in [a, b, c]) \quad (18)$$

And then these output channel-wise graphs are expanded spatially and applied directly on each input feature X_i^a , X_i^b and X_i^c , obtaining three refined features \widehat{X}_i^a , \widehat{X}_i^b and \widehat{X}_i^c , respectively.

$$\widehat{X}_i^\alpha = X_i^\alpha * Expand(\widehat{G}_i^\alpha) + X_i^\alpha \quad (\alpha \in [a, b, c]) \quad (19)$$

Finally, we concatenate the three refined features and adopt a conv1x1 operator to reduce the dimension and generate the output fused feature Y_i^{Fused} .

$$Y_i^{Fused} = Conv1x1(Concat(\widehat{X}_i^\alpha)) \quad (\alpha \in [a, b, c]) \quad (20)$$

3.6. Loss Function

The Cross Entropy (CE) loss \mathcal{L}_{CE} is used as the loss function of our GCC-UNet, which is defined as

$$\mathcal{L}_{CE}(p, q) = - \sum_{k=1}^N p_k * log(q_k) \quad (21)$$

4. Datasets and Materials

4.1. Retinal Fundus Datasets

Our GCC-UNet model was evaluated on three publicly available retinal vessel datasets, namely DRIVE [57], STARE [58], and CHASEDB1 [20].

The DRIVE dataset consists of 40 pairs of fundus images with a unified size of 565×584 pixels, where 20 pairs are used as training data and the remaining pairs as the test data. The STARE dataset comprises 20 pairs of

fundus images and their corresponding labels with a size of 700×605 pixels. The first 10 pairs are used as the training dataset, and the remaining pairs are used as the test dataset. The CHASEDB1 dataset contains 28 pairs of fundus scans and their labels with a resolution of 999×960 pixels, where the first 20 pairs are used as the training dataset and the remaining 8 pairs are used as the test set.

Furthermore, to comprehensively evaluate our proposed GCC-UNet model, we also tested it on some challenging datasets, including AV-WIDE [18], UoA-DR [59], and UK Biobank [60]. It should be noted that the model used for testing on these datasets was trained on the DRIVE dataset.

4.2. Evaluation Metrics

We evaluated our model with some classical metrics, including F1 score (F1), accuracy (Acc), sensitivity (SE), specificity (SP), and area under the ROC curve (AUROC), which are defined as follows:

$$SE = Rec = \frac{TP}{TP + FN} \quad SP = \frac{TN}{TN + FP}$$

$$(22)$$

$$F1 = 2 \times \frac{Pre \times Rec}{Pre + Rec} \quad Acc = \frac{TP + TN}{TP + TN + FP + FN}$$

where TP , TN , FP , and FN represent the number of true positive, true negative, false positive, and false negative pixels, respectively. Pre and Rec mean the precision and recall metrics, respectively. In addition, some advanced metrics proposed by Gegundez et al. [61] were also adopted to evaluate our model, including connectivity (C), overlapping area (A), consistency of vessel length (L), and the overall metric (F). The overall metric (F) is

defined as

$$F = C \times A \times L \quad (23)$$

Furthermore, rSE, rSP and rAcc proposed in [62] were also adopted to act as indicators for the evaluation, as well as the Matthews Correlation Coefficient (Mcc) [63].

5. Experiments

5.1. Implementation details

The GCC-UNet model was implemented using the PyTorch framework and trained on a TITAN XP GPU. During the training process, we used the Adam optimizer. The model was trained with a batch size of 32 over a total of 60 epochs. The early stopping strategy was adopted with a patience of 10 epochs. When calculating performance metrics, we only take pixels in the field of view (FOV) into consideration.

5.2. Overall comparison with other methods

We conducted comprehensive comparison experiments to demonstrate the performance of our proposed GCC-UNet model. The results presented in Tables 1, 2, 3, and 4 show that our method outperforms numerous state-of-the-art methods on the DRIVE [57], STARE [58], and CHASEDB1 [20] datasets, in terms of both traditional and advanced metrics. Furthermore, as shown in Fig. 7 and 8, our method also exhibits superior visual performance compared with other methods, particularly in detecting thin vessels. These results provide further evidence of the effectiveness of our approach and its ability to capture global context and improve the continuity of vessels.

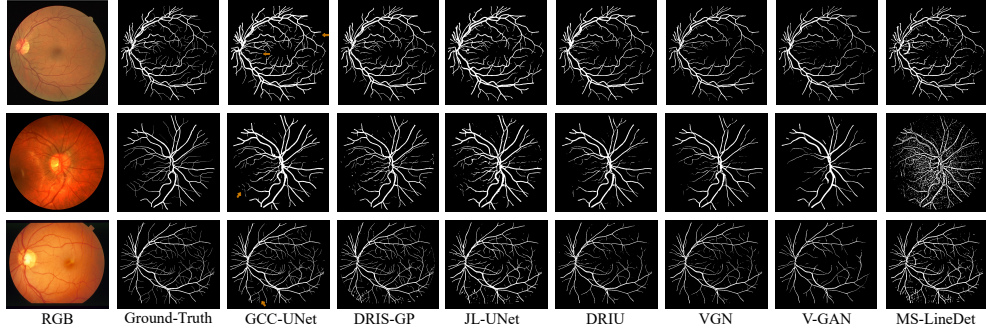


Figure 7: Visual comparison with other state-of-the-art methods on DRIVE(the first row), CHASEDB1(the second row) and STARE(the third row) datasets.

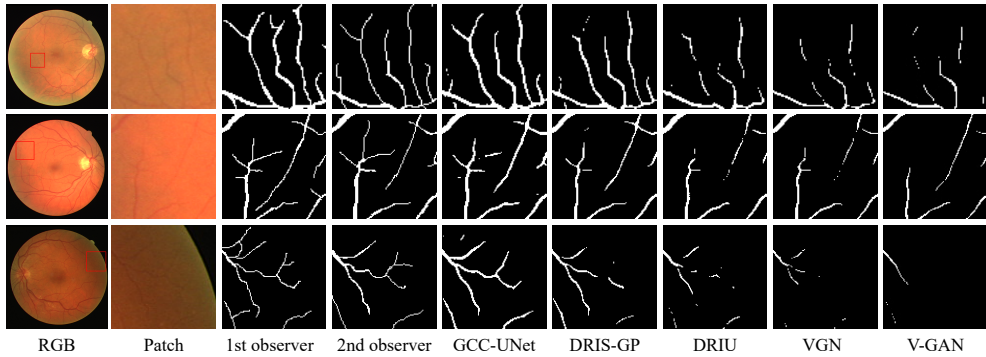


Figure 8: Visual comparison with other methods in terms of thin vessels.

Table 1: Quantitative evaluation against other leading methods on **DRIVE**. Red: the best, Blue: the second best.

| Method | F1 | Se | Sp | Acc | AUROC |
|------------------------|--------------|--------------|--------------|--------------|--------------|
| 2nd observer [57] | N.A | 77.60 | 97.24 | 94.72 | N.A |
| HED [14] | 80.89 | 76.27 | 98.01 | 95.24 | 97.58 |
| DeepVessel [24] | N.A | 76.12 | 97.68 | 95.23 | 97.52 |
| Orlando et al. [19] | N.A | 78.97 | 96.84 | 94.54 | 95.06 |
| JL-UNet [37] | N.A | 76.53 | 98.18 | 95.42 | 97.52 |
| CC-Net [8] | N.A | 76.25 | 98.09 | 95.28 | 96.78 |
| Att UNet [33] | 82.32 | 79.46 | 97.89 | 95.64 | 97.99 |
| Yan et al. [64] | N.A | 76.31 | 98.20 | 95.33 | 97.50 |
| BTS-DSN [28] | 82.08 | 78.00 | 98.06 | 95.51 | 97.96 |
| CTF-Net [38] | 82.41 | 78.49 | 98.13 | 95.67 | 97.88 |
| CSU-Net [7] | 82.51 | 80.71 | 97.82 | 95.65 | 98.01 |
| RCAR-UNet [40] | 80.47 | 74.87 | 98.36 | 95.37 | N.A |
| GCC-UNet (Ours) | 82.78 | 80.32 | 98.21 | 95.74 | 98.13 |

Table 2: Quantitative comparison with other methods on **STARE**.

| Method | F1 | Se | Sp | Acc | AUROC |
|------------------------|--------------|--------------|--------------|--------------|--------------|
| HED [14] | 82.68 | 80.76 | 98.22 | 96.41 | 98.24 |
| Orlando et al. [19] | N.A | 76.80 | 97.38 | 95.19 | 95.70 |
| JL-UNet [37] | N.A | 75.81 | 98.46 | 96.12 | 98.01 |
| Att UNet [33] | 81.36 | 80.67 | 98.16 | 96.32 | 98.33 |
| CC-Net [8] | N.A | 77.09 | 98.48 | 96.33 | 97.00 |
| Dense UNet [34] | 82.32 | 78.59 | 98.42 | 96.44 | 98.47 |
| Yan et al. [64] | N.A | 77.35 | 98.57 | 96.38 | 98.33 |
| DUNet [35] | 82.30 | 78.92 | 98.16 | 96.34 | 98.43 |
| RCAR-UNet [40] | 78.50 | 69.79 | 99.05 | 95.94 | N.A |
| GCC-UNet (Ours) | 82.82 | 78.06 | 98.77 | 96.58 | 98.56 |

Table 3: Quantitative comparison with other methods on **CHASEDB1**.

| Method | F1 | Se | Sp | Acc | AUROC |
|------------------------|--------------|--------------|--------------|--------------|--------------|
| 2nd observer [57] | N.A | 81.05 | 97.11 | 95.45 | N.A |
| HED [14] | 78.15 | 75.16 | 98.05 | 95.97 | 97.96 |
| DeepVessel [24] | N.A | 74.12 | 97.01 | 96.09 | 97.90 |
| Orlando et al. [19] | N.A | 75.65 | 96.55 | 94.67 | 94.78 |
| JL-UNet [37] | N.A | 76.33 | 98.09 | 96.10 | 97.81 |
| Att UNet [33] | 80.12 | 80.10 | 98.04 | 96.42 | 98.40 |
| Dense UNet [34] | 79.01 | 78.93 | 97.92 | 96.11 | 98.35 |
| Yan et al. [64] | N.A | 76.41 | 98.06 | 96.07 | 97.76 |
| BTS-DSN [28] | 79.83 | 78.88 | 98.01 | 96.27 | 98.40 |
| DUNet [35] | 79.32 | 77.35 | 98.01 | 96.18 | 98.39 |
| RCAR-UNet [40] | 74.70 | 74.75 | 97.98 | 95.66 | N.A |
| GCC-UNet (Ours) | 80.86 | 81.23 | 98.15 | 96.59 | 98.50 |

Table 4: Quantitative comparison with other methods in terms of metrics in [62] on **DRIVE** dataset.

| Method | F | C | A | L | rSe | rSp | rAcc | Mcc |
|-----------------|--------------|--------------|--------------|--------------|--------------|--------------|--------------|--------------|
| 2nd observer | 83.75 | 100 | 93.98 | 89.06 | 85.84 | 99.19 | 95.74 | 76.00 |
| HED [14] | 80.09 | 99.75 | 90.06 | 89.11 | 71.57 | 95.11 | 89.08 | 66.00 |
| DRIU [25] | 80.43 | 99.56 | 91.52 | 88.23 | 82.36 | 96.85 | 93.13 | 71.61 |
| DeepVessel [24] | 61.74 | 99.60 | 84.23 | 73.38 | 54.93 | 99.78 | 88.32 | 73.34 |
| V-GAN [27] | 84.82 | 99.64 | 94.69 | 89.84 | 80.77 | 99.63 | 94.76 | 80.24 |
| JL-UNet [37] | 81.06 | 99.61 | 93.08 | 87.35 | 76.11 | 99.57 | 93.53 | 78.98 |
| SWT-FCN [29] | 83.92 | 99.73 | 94.36 | 89.11 | 79.63 | 99.64 | 94.48 | 80.53 |
| DeepDyn [30] | 84.53 | 90.70 | 94.58 | 89.61 | 81.52 | 99.44 | 94.82 | 80.02 |
| DAP [65] | 82.55 | 99.72 | 93.74 | 88.24 | 78.57 | 99.57 | 94.15 | 79.00 |
| DRIS-GP [31] | 84.94 | 99.68 | 94.91 | 89.74 | 80.22 | 99.64 | 94.66 | 81.84 |
| GCC-UNet | 85.83 | 99.75 | 95.10 | 90.46 | 82.60 | 99.17 | 95.06 | 80.27 |

Table 5: Comparison between the vanilla Capsule Conv (Cap Conv) in [48] and our Graph Capsule Conv (GC Conv) on DRIVE.

| Method | F1 | Se | Sp | Acc | AUROC |
|-----------------------------|--------------|--------------|--------------|--------------|--------------|
| Baseline (UNet) [32] | 81.76 | 78.36 | 98.03 | 95.56 | 97.86 |
| + Capsule Conv [48] | 81.19 | 78.07 | 98.12 | 95.53 | 97.81 |
| + GC Conv (Proposed) | 82.01 | 78.12 | 98.18 | 95.63 | 97.93 |

5.3. Comparison and ablation study of individual module

5.3.1. Comparison and ablation analysis between the proposed GC Conv and plain Capsule Conv

To advance beyond the limitations of vanilla capsule convolution [48], we introduce the Graph Capsule Convolution (GC Conv), designed to capture the intricate interdependencies among channels, capsules, and even atomic units. In our experiments, we substituted the conventional convolution operations with both capsule convolution (Cap Conv) [48] and our innovative GC Conv within the U-Net framework. As illustrated in Table 5, the performance notably declined when vanilla convolutions were replaced with Cap Conv, whereas our GC Conv demonstrated substantial improvements.

This enhancement is attributed to the fact that while capsule convolution primarily focuses on capturing global features such as relative positions, orientations, and colors of vessels, it does not explicitly model the interactions among these global attributes. For example, capillaries typically exhibit lighter colors and are found at terminal branches (positions), with more intricate orientations. In contrast, GC Conv excels by modeling the relationships among these characteristics and learning their correlations in a graph-based framework, thereby capturing more comprehensive and nuanced feature interdependencies.

5.3.2. Comparison and ablation analysis between the proposed SGAF and other fusion modules

We conducted an extensive series of experiments to assess the efficacy of our proposed Selective Graph Attention Fusion (SGAF) module in comparison to other fusion strategies. Table 6 presents the performance metrics for integrating local features with various types of global features. These global features were extracted using the conventional Capsule Convolution (Cap Conv) with dynamic routing [48] and our novel Graph Capsule Convolution (GC Conv) with graph-based dynamic routing. Alongside SGAF, we also assessed the performance of vanilla Conv1x1 [21] and Selective Kernel Attention (SK) [66] as alternative fusion modules.

The results in Table 6 indicate that Conv1x1 was suboptimal for fusing local and global features, failing to distinguish between beneficial channels in these feature types. Conversely, SK Attention demonstrated effective feature fusion across different mechanisms, achieving commendable performance. Nonetheless, our SGAF module surpassed SK Attention by a substantial margin. Additionally, GC Conv significantly outperformed Cap Conv in extracting global contextual features while utilizing the same fusion module.

We also investigated various operational modes, including the serial and parallel configurations depicted in Fig. 9, for combining CNN Conv and Capsule Conv. Our findings reveal that the serial mode outperforms the parallel mode. Given that both Cap Conv and GC Conv cannot directly extract global information from raw images, the most effective strategy involves initially using vanilla CNN convolutions to extract features, followed

by capsule convolutions to further refine global contextual information from the CNN features. This approach is then complemented by fusing local and global features through skip connections.

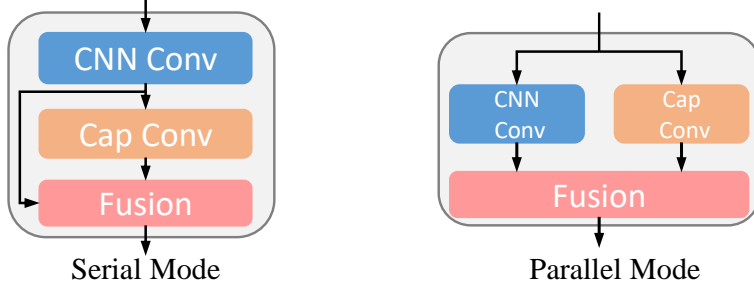


Figure 9: Different modes for combining CNN Conv and Capsule Conv.

Table 6: Comparison between our SGAF and other fusion modules (Conv1x1[21], SK Attention[66]) on DRIVE.

| Method | F1 | Se | Sp | Acc | AUROC |
|---|--------------|--------------|--------------|--------------|--------------|
| Baseline (UNet) [32] | 81.76 | 78.36 | 98.03 | 95.56 | 97.86 |
| Baseline (Capsule UNet) [48] | 81.19 | 78.07 | 98.12 | 95.53 | 97.81 |
| CAPSULE / FUSION | F1 | Se | Sp | Acc | AUC |
| Cap Conv[48] / Conv1x1[21] | 81.42 | 77.96 | 97.79 | 95.52 | 97.82 |
| Cap Conv[48] / SK[66] | 82.12 | 78.16 | 97.76 | 95.65 | 98.01 |
| Cap Conv[48] / <u>SGAF</u> | 82.30 | 78.98 | 98.18 | 95.67 | 98.04 |
| <u>GC Conv</u> / Conv1x1[21] | 81.82 | 78.53 | 97.92 | 95.59 | 97.87 |
| <u>GC Conv</u> / SK[66] | 82.23 | 78.86 | 97.91 | 95.68 | 98.03 |
| <u>GC Conv</u> / <u>SGAF</u> (Parallel) | 81.75 | 79.36 | 98.05 | 95.64 | 97.99 |
| <u>GC Conv</u> / <u>SGAF</u> (Serial) | 82.42 | 79.45 | 98.11 | 95.70 | 98.07 |

5.3.3. Comparison and ablation analysis between our proposed BGA and other attention modules in the bottleneck

We conducted a series of experiments to evaluate the performance of our proposed Bottleneck Graph Attention (BGA) module in comparison with

several prominent attention mechanisms. As demonstrated in Table 7, our BGA module consistently outperforms other well-established attention modules, including SE [67], CBAM [68], Non-Local [11], and Self-Attention [10]. Additionally, both our Channel Graph Attention (CGA) and Spatial Attention (SGA) components achieve notable performance.

The superior performance of our BGA module is attributed to its ability to model channel relationships through CGA by constructing and learning a graph representation. Furthermore, BGA leverages SGA to effectively distinguish vessels from the background and enhance vessel continuity by learning the connectivity among vessel nodes. This dual approach enables more accurate vessel segmentation and continuity preservation, highlighting the efficacy of our proposed attention mechanism.

Table 7: Comaprison and ablation study of the proposed BGA and other attention modules on DRIVE.

| Method | F1 | Se | Sp | Acc | AUROC |
|-------------------------|--------------|--------------|--------------|--------------|--------------|
| Baseline (UNet) [32] | 81.76 | 78.36 | 98.03 | 95.56 | 97.86 |
| + SE [67] | 81.81 | 79.03 | 97.77 | 95.60 | 97.90 |
| + CBAM [68] | 81.06 | 78.85 | 97.87 | 95.61 | 97.89 |
| + Non-Local [11] | 81.75 | 78.98 | 97.76 | 95.61 | 97.91 |
| + Self-Attention [10] | 82.03 | 79.45 | 97.96 | 95.64 | 97.93 |
| + CGA (Proposed) | 82.18 | 79.32 | 98.00 | 95.64 | 97.93 |
| + SGA (Proposed) | 82.11 | 79.89 | 97.95 | 95.64 | 97.93 |
| + BGA (Proposed) | 82.25 | 79.65 | 98.05 | 95.67 | 97.94 |

5.3.4. Comparison and ablation analysis between our proposed MSGF and other multi-scale fusion modules

We conducted a series of experiments to assess the efficacy of our proposed Multi-Scale Graph Fusion (MSGF) module against other multi-scale fusion

techniques, including the vanilla Conv1x1 and the fusion module described in [69]. Furthermore, we evaluated three distinct modes of our MSGF module: Individual (applying separate graph convolutions to each of the three different scales of input graphs), Concat (concatenating the graphs from the three input features and processing them with a single graph convolution), and Shared (feeding the graphs from the input features into a shared graph convolution).

As illustrated in Table 8, all three MSGF modes outperformed the other fusion modules. Among these, the Shared mode demonstrated superior performance with fewer parameters and reduced computational costs. This advantage arises because the Shared mode processes the graphs from the three scales using a single graph convolution, enabling the convolution operator to assimilate all relevant information and features concurrently. Additionally, since the features at different scales are derived from the same fundus image and are presumed to follow a similar graph pattern, utilizing a single graph convolution aligns the graph representations across these scales. This approach facilitates the integration and complementarity of information from all scales within one shared graph convolution, thereby enhancing overall performance.

5.4. Overall ablation study of different fashions

Following a comprehensive ablation analysis of each proposed module, we conducted an overall ablation study in three different configurations: local-only, global-only, and global-local fusion. As detailed in Table 9, we examined four configurations: local-only, vanilla global-only, improved global-only, and global-local fusion.

Table 8: Ablation study of the proposed MSGF on DRIVE.

| Method | F1 | Se | Sp | Acc | AUROC |
|--------------------------|--------------|--------------|--------------|--------------|--------------|
| Baseline (UNet) [32] | 81.76 | 78.36 | 98.03 | 95.56 | 97.86 |
| + Fusion via Conv1x1[21] | 81.69 | 78.88 | 97.89 | 96.59 | 97.89 |
| + Fusion module in [69] | 81.86 | 78.54 | 97.95 | 96.62 | 97.91 |
| + MSGF (Individual) | 82.03 | 78.84 | 98.02 | 96.64 | 97.93 |
| + MSGF (Concat) | 81.95 | 79.14 | 97.98 | 96.64 | 97.93 |
| + MSGF (Shared) | 82.15 | 79.23 | 98.08 | 95.68 | 97.94 |

Table 9: Overall ablation study of each proposed module on DRIVE.

| Method (Local-only) | F1 | Se | Sp | Acc | AUROC |
|------------------------------------|-------|-------|-------|-------|-------|
| Local UNet (Plain Conv) [32] | 81.76 | 78.36 | 98.03 | 95.56 | 97.86 |
| + BGA | 82.25 | 79.65 | 98.05 | 95.67 | 97.94 |
| + BGA + MSGF | 82.42 | 80.04 | 98.09 | 95.70 | 98.01 |
| Method (Vanilla Global-only) | F1 | Se | Sp | Acc | AUC |
| Global UNet (Capsule Conv) [48] | 81.19 | 78.07 | 98.12 | 95.53 | 97.81 |
| + BGA | 81.43 | 78.85 | 98.05 | 95.58 | 97.87 |
| + BGA + MSGF | 81.93 | 79.32 | 98.12 | 95.63 | 97.93 |
| Method (Improved Global-only) | F1 | Se | Sp | Acc | AUC |
| Global UNet (GC Conv) | 82.01 | 78.12 | 98.18 | 95.63 | 97.93 |
| + BGA | 82.25 | 79.65 | 98.05 | 95.67 | 97.98 |
| + BGA + MSGF | 82.36 | 80.04 | 98.09 | 95.70 | 98.03 |
| Method (Global-Local Fusion) | F1 | Se | Sp | Acc | AUC |
| Fusion UNet (Plain Conv + GC Conv) | 82.42 | 79.45 | 98.11 | 95.70 | 98.07 |
| + BGA | 82.61 | 80.02 | 98.16 | 95.71 | 98.10 |
| + BGA + MSGF | 82.78 | 80.32 | 98.21 | 95.74 | 98.13 |

In the local-only configuration, we used the vanilla U-Net as the baseline, which comprises basic convolutional blocks capable of capturing only local features. When augmented with our proposed Bottleneck Graph Attention (BGA) and Multi-Scale Graph Fusion (MSGF) modules, the model achieved a notable performance improvement, attaining 98.01% AUROC.

For the vanilla global-only configuration, we substituted the standard convolution layers in U-Net with vanilla capsule convolution [48] to create a new U-Net model focused solely on capturing global features. The performance of this global-only U-Net was inferior to that of the local-only configuration. However, when enhanced with our BGA and MSGF modules, the model’s performance saw a significant boost. Furthermore, replacing the vanilla capsule convolution with our Graph Capsule Convolution (GC Conv) led to even better performance, demonstrating that GC Conv surpasses the vanilla capsule convolution [48] in modeling contextual features and that BGA and MSGF effectively complement our GC Conv.

Finally, experiments with the global-local fusion baseline revealed that this configuration outperforms both the local-only and global-only models. This result underscores the substantial benefit of integrating both local and global features for retinal vessel segmentation, affirming the effectiveness of our fusion approach.

5.5. Comparison study on challenging test sets

To evaluate the generalization capabilities of our GCC-UNet model, we performed experiments on several challenging datasets, including AV-WIDE [18], UoA-DR [59], and UK Biobank [60]. For comparison, all models were trained from scratch on the DRIVE dataset.

Our results, as illustrated in Fig. 10 and 11, reveal that GCC-UNet surpasses state-of-the-art methods such as DRIU and DRIS-GP, and offers a substantial improvement over the baseline U-Net. In particular, the UK Biobank test results (Fig. 11) highlight areas where thin vessels are obscured by opacities, which are notoriously difficult to detect even by human experts. Despite these challenges, our GCC-UNet model effectively identified these blurred and occluded vessels, demonstrating its superior performance and robustness.

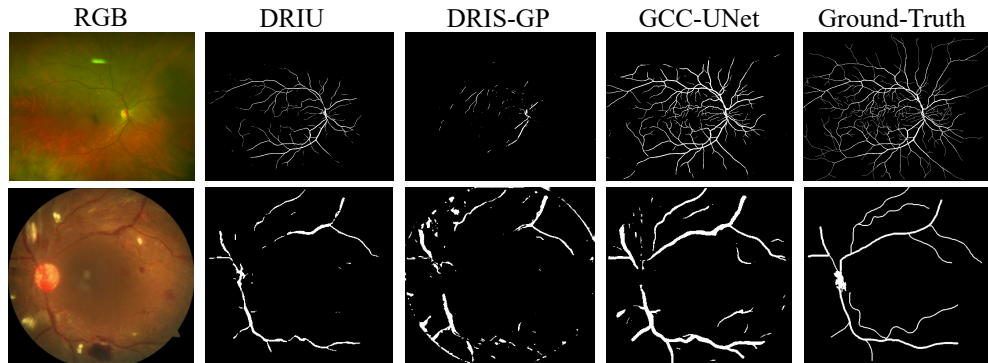


Figure 10: Visual comparison on the AV-WIDE (1st row) and UoA-DR (2nd row) datasets.

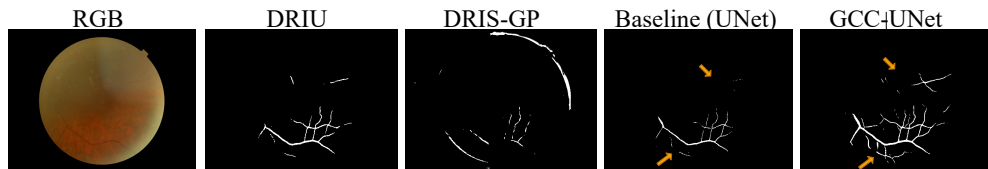


Figure 11: Visual comparison on the UK Biobank dataset.

5.6. Comparison of model size, parameters and flops

To highlight the efficiency of our GCC-UNet, we compared it with several UNet-based methods, including vanilla UNet [32], Attention U-Net [33],

Table 10: Comparison of Model Size, Parameters and Flops on DRIVE.

| Method | UNet | Att UNet | Dense UNet | DUNet | GCC-UNet |
|------------|------|----------|------------|-------|----------|
| Size (M) | 3.4 | 7.1 | 11.0 | 7.4 | 5.5 |
| Params (M) | 0.28 | 0.29 | 0.31 | 0.43 | 0.39 |
| Flops (G) | 0.14 | 0.15 | 0.44 | 0.23 | 0.18 |

Dense U-Net [34], and Deformable U-Net [35], evaluating model size, parameter count, and computational complexity (FLOPs).

As presented in Table 10, GCC-UNet outperforms many existing UNet-based models while maintaining a compact parameter size and relatively small model footprint. This indicates that our GCC-UNet strikes an effective balance between computational efficiency and model performance, providing both high efficacy and manageable resource requirements.

5.7. The potential of our method: Extend the ability of geometric modeling to boundary detection tasks

We propose integrating graph-based and capsule-based approaches into medical image segmentation tasks, particularly those requiring precise boundary detection, such as optic disc segmentation, brain tumor segmentation, and biological cell segmentation. Our Bottleneck Graph Attention (BGA) module shows significant promise for enhancing boundary continuity. For instance, the sign function in the Spatial Graph Attention (SGA) can be employed to approximate boundary locations, followed by constructing a graph to reinforce continuity. Alternatively, the use of oriented kernels [31] [39] can further enhance boundary continuity.

Looking ahead, a promising direction for future work is to incorporate orientation modeling into graph construction processes. This enhancement could further improve the continuity of vessels and object boundaries, thereby

advancing the accuracy and effectiveness of medical image segmentation tasks.

6. Discussion

Our proposed GCC-UNet has achieved impressive results in retinal vessel segmentation by effectively integrating global context, part-to-whole relationships, and local-global fusion, while also enhancing vessel continuity. Notably, the model maintains a relatively compact parameter count of just 5.48M. However, there are inherent limitations in our approach. As highlighted by [48], although capsule convolution facilitates the capture of global context, it also substantially increases the model’s computational cost, leading to slower inference speeds. This challenge is a fundamental characteristic of capsule convolution.

While our Graph Capsule Convolution (GC Conv) significantly enhances the efficacy of capsule convolution, it does not address the issue of increased computational cost or improved inference speed. Future work will focus on developing techniques to accelerate capsule convolution. Additionally, exploring the application of directed graph neural networks [70] in medical image segmentation tasks could be an exciting avenue for improving the continuity of curvilinear boundaries, further advancing the field.

7. Conclusion

In this study, we introduce a novel model for retinal vessel segmentation that combines global and local fusion within a U-Net framework, incorporating vanilla, graph, and capsule convolutions in a unified approach. This represents the first attempt to integrate these diverse convolutional techniques.

Specifically, our model utilizes capsule convolution to capture global contextual information and graph convolution to model vessel connectivity and enhance continuity. Our Graph Capsule Convolution (GC Conv) advances the traditional capsule convolution by improving its effectiveness. Additionally, the Selective Graph Attention Fusion (SGAF) module facilitates the integration of features across different domains (CNN, Graph, and Capsule). The Bottleneck Graph Attention (BGA) module enhances vessel continuity through a divide-and-conquer strategy, while the Multi-Scale Graph Fusion (MSGF) module effectively manages multi-scale feature fusion. Crucially, the modules developed in this study are versatile and can be extended to a variety of applications beyond vessel segmentation. These include MRI tumor segmentation, geometric modeling of medical images, and both semantic and instance segmentation tasks.

References

- [1] Tao Li, Wang Bo, Chunyu Hu, Hong Kang, Hanruo Liu, Kai Wang, and Huazhu Fu. Applications of deep learning in fundus images: A review. *Medical Image Analysis*, 69:101971, 2021.
- [2] Shahzad Akbar, Muhammad Sharif, Muhammad Usman Akram, Tanzila Saba, Toqueer Mahmood, and Mahyar Kolivand. Automated techniques for blood vessels segmentation through fundus retinal images: A review. *Microscopy research and technique*, 82(2):153–170, 2019.
- [3] Xi Lin, Xinxu Wei, Shixuan Zhao, and Yongjie Li. Vascular skeleton deformation evaluation based on the metric of sinkhorn distance. In 2024

IEEE International Symposium on Biomedical Imaging (ISBI), pages 1–5. IEEE, 2024.

- [4] João VB Soares, Jorge JG Leandro, Roberto M Cesar, Herbert F Jelinek, and Michael J Cree. Retinal vessel segmentation using the 2-d gabor wavelet and supervised classification. IEEE Transactions on medical Imaging, 25(9):1214–1222, 2006.
- [5] Subhasis Chaudhuri, Shankar Chatterjee, Norman Katz, Mark Nelson, and Michael Goldbaum. Detection of blood vessels in retinal images using two-dimensional matched filters. IEEE Transactions on medical imaging, 8(3):263–269, 1989.
- [6] José Ignacio Orlando and Matthew Blaschko. Learning fully-connected crfs for blood vessel segmentation in retinal images. In international conference on medical image computing and computer-assisted intervention, pages 634–641. Springer, 2014.
- [7] Bo Wang, Shengpei Wang, Shuang Qiu, Wei Wei, Haibao Wang, and Huiguang He. Csu-net: A context spatial u-net for accurate blood vessel segmentation in fundus images. IEEE Journal of Biomedical and Health Informatics, 25(4):1128–1138, 2020.
- [8] Shouting Feng, Zhongshuo Zhuo, Daru Pan, and Qi Tian. Ccnet: A cross-connected convolutional network for segmenting retinal vessels using multi-scale features. Neurocomputing, 392:268–276, 2020.
- [9] Fisher Yu and Vladlen Koltun. Multi-scale context aggregation by dilated convolutions. arXiv preprint arXiv:1511.07122, 2015.

- [10] Ashish Vaswani, Noam Shazeer, Niki Parmar, Jakob Uszkoreit, Llion Jones, Aidan N Gomez, Łukasz Kaiser, and Illia Polosukhin. Attention is all you need. *Advances in neural information processing systems*, 30, 2017.
- [11] Xiaolong Wang, Ross Girshick, Abhinav Gupta, and Kaiming He. Non-local neural networks. In *Proceedings of the IEEE conference on computer vision and pattern recognition*, pages 7794–7803, 2018.
- [12] Bob Zhang, Lin Zhang, Lei Zhang, and Fakhri Karray. Retinal vessel extraction by matched filter with first-order derivative of gaussian. *Computers in biology and medicine*, 40(4):438–445, 2010.
- [13] Benjun Yin, Huating Li, Bin Sheng, Xuhong Hou, Yan Chen, Wen Wu, Ping Li, Ruimin Shen, Yuqian Bao, and Weiping Jia. Vessel extraction from non-fluorescein fundus images using orientation-aware detector. *Medical image analysis*, 26(1):232–242, 2015.
- [14] Saining Xie and Zhuowen Tu. Holistically-nested edge detection. In *Proceedings of the IEEE international conference on computer vision*, pages 1395–1403, 2015.
- [15] Elisa Ricci and Renzo Perfetti. Retinal blood vessel segmentation using line operators and support vector classification. *IEEE transactions on medical imaging*, 26(10):1357–1365, 2007.
- [16] Uyen TV Nguyen, Alauddin Bhuiyan, Laurence AF Park, and Kotagiri Ramamohanarao. An effective retinal blood vessel segmentation

- method using multi-scale line detection. *Pattern recognition*, 46(3):703–715, 2013.
- [17] Tariq M Khan, Mohammad AU Khan, Naveed Ur Rehman, Khuram Naveed, Imran Uddin Afridi, Syed Saud Naqvi, and Imran Raazak. Width-wise vessel bifurcation for improved retinal vessel segmentation. *Biomedical Signal Processing and Control*, 71:103169, 2022.
- [18] Rolando Estrada, Michael J Allingham, Priyatham S Mettu, Scott W Cousins, Carlo Tomasi, and Sina Farsiu. Retinal artery-vein classification via topology estimation. *IEEE transactions on medical imaging*, 34(12):2518–2534, 2015.
- [19] José Ignacio Orlando, Elena Prokofyeva, and Matthew B Blaschko. A discriminatively trained fully connected conditional random field model for blood vessel segmentation in fundus images. *IEEE transactions on Biomedical Engineering*, 64(1):16–27, 2016.
- [20] Muhammad Moazam Fraz, Paolo Remagnino, Andreas Hoppe, Bunyarit Uyyanonvara, Alicja R Rudnicka, Christopher G Owen, and Sarah A Barman. An ensemble classification-based approach applied to retinal blood vessel segmentation. *IEEE Transactions on Biomedical Engineering*, 59(9):2538–2548, 2012.
- [21] Karen Simonyan and Andrew Zisserman. Very deep convolutional networks for large-scale image recognition. *arXiv preprint arXiv:1409.1556*, 2014.

- [22] Kaiming He, Xiangyu Zhang, Shaoqing Ren, and Jian Sun. Deep residual learning for image recognition. In Proceedings of the IEEE conference on computer vision and pattern recognition, pages 770–778, 2016.
- [23] Xinxu Wei, Xiangke Niu, Xianshi Zhang, and Yongjie Li. Deep pneumonia: Attention-based contrastive learning for class-imbalanced pneumonia lesion recognition in chest x-rays. In 2022 IEEE International Conference on Big Data (Big Data), pages 5361–5369. IEEE, 2022.
- [24] Huazhu Fu, Yanwu Xu, Stephen Lin, Damon Wing Kee Wong, and Jiang Liu. Deepvessel: Retinal vessel segmentation via deep learning and conditional random field. In International conference on medical image computing and computer-assisted intervention, pages 132–139. Springer, 2016.
- [25] Kevis-Kokitsi Maninis, Jordi Pont-Tuset, Pablo Arbeláez, and Luc Van Gool. Deep retinal image understanding. In International conference on medical image computing and computer-assisted intervention, pages 140–148. Springer, 2016.
- [26] Seung Yeon Shin, Soochahn Lee, Il Dong Yun, and Kyoung Mu Lee. Deep vessel segmentation by learning graphical connectivity. Medical image analysis, 58:101556, 2019.
- [27] Jaemin Son, Sang Jun Park, and Kyu-Hwan Jung. Retinal vessel segmentation in fundoscopic images with generative adversarial networks. arXiv preprint arXiv:1706.09318, 2017.

- [28] Song Guo, Kai Wang, Hong Kang, Yujun Zhang, Yingqi Gao, and Tao Li. Bts-dsn: Deeply supervised neural network with short connections for retinal vessel segmentation. *International journal of medical informatics*, 126:105–113, 2019.
- [29] Américo Oliveira, Sergio Pereira, and Carlos A Silva. Retinal vessel segmentation based on fully convolutional neural networks. *Expert Systems with Applications*, 112:229–242, 2018.
- [30] Aashis Khanal and Rolando Estrada. Dynamic deep networks for retinal vessel segmentation. *Frontiers in Computer Science*, page 35, 2020.
- [31] Venkateswararaao Cherukuri, Vijay Kumar Bg, Raja Bala, and Vishal Monga. Deep retinal image segmentation with regularization under geometric priors. *IEEE Transactions on Image Processing*, 29:2552–2567, 2019.
- [32] Olaf Ronneberger, Philipp Fischer, and Thomas Brox. U-net: Convolutional networks for biomedical image segmentation. In *International Conference on Medical image computing and computer-assisted intervention*, pages 234–241. Springer, 2015.
- [33] Ozan Oktay, Jo Schlemper, Loic Le Folgoc, Matthew Lee, Matthias Heinrich, Kazunari Misawa, Kensaku Mori, Steven McDonagh, Nils Y Hammerla, Bernhard Kainz, et al. Attention u-net: Learning where to look for the pancreas. *arXiv preprint arXiv:1804.03999*, 2018.
- [34] Xiaomeng Li, Hao Chen, Xiaojuan Qi, Qi Dou, Chi-Wing Fu, and Pheng-Ann Heng. H-denseunet: hybrid densely connected unet for liver

- and tumor segmentation from ct volumes. *IEEE transactions on medical imaging*, 37(12):2663–2674, 2018.
- [35] Qiangguo Jin, Zhaopeng Meng, Tuan D Pham, Qi Chen, Leyi Wei, and Ran Su. Dunet: A deformable network for retinal vessel segmentation. *Knowledge-Based Systems*, 178:149–162, 2019.
- [36] Changlu Guo, Márton Szemenyei, Yugen Yi, Wenle Wang, Buer Chen, and Changqi Fan. Sa-unet: Spatial attention u-net for retinal vessel segmentation. In *2020 25th international conference on pattern recognition (ICPR)*, pages 1236–1242. IEEE, 2021.
- [37] X. Yang Z. Yan and K. Cheng. Joint segment-level and pixel-wise losses for deep learning based retinal vessel segmentation. *IEEE Transactions on Biomedical Engineering*, 65(9):1912–1923, 2018.
- [38] Kun Wang, Xiaohong Zhang, Sheng Huang, Qiuli Wang, and Feiyu Chen. Ctf-net: Retinal vessel segmentation via deep coarse-to-fine supervision network. In *2020 IEEE 17th International Symposium on Biomedical Imaging (ISBI)*, pages 1237–1241. IEEE, 2020.
- [39] Xinxu Wei, Kaifu Yang, Danilo Bzdok, and Yongjie Li. Orientation and context entangled network for retinal vessel segmentation. *Expert Systems with Applications*, 217:119443, 2023.
- [40] Weiping Ding, Ying Sun, Jiashuang Huang, Hengrong Ju, Chongsheng Zhang, Guang Yang, and Chin-Teng Lin. Rcar-unet: Retinal vessel segmentation network algorithm via novel rough attention mechanism. *Information Sciences*, 657:120007, 2024.

- [41] Si Zhang, Hanghang Tong, Jiejun Xu, and Ross Maciejewski. Graph convolutional networks: a comprehensive review. *Computational Social Networks*, 6(1):1–23, 2019.
- [42] Thomas N Kipf and Max Welling. Semi-supervised classification with graph convolutional networks. *arXiv preprint arXiv:1609.02907*, 2016.
- [43] Li Zhang, Xiangtai Li, Anurag Arnab, Kuiyuan Yang, Yunhai Tong, and Philip HS Torr. Dual graph convolutional network for semantic segmentation. *arXiv preprint arXiv:1909.06121*, 2019.
- [44] Jin Ye, Junjun He, Xiaojiang Peng, Wenhao Wu, and Yu Qiao. Attention-driven dynamic graph convolutional network for multi-label image recognition. In *Computer Vision–ECCV 2020: 16th European Conference, Glasgow, UK, August 23–28, 2020, Proceedings, Part XXI* 16, pages 649–665. Springer, 2020.
- [45] Yanda Meng, Hongrun Zhang, Dongxu Gao, Yitian Zhao, Xiaoyun Yang, Xuesheng Qian, Xiaowei Huang, and Yalin Zheng. Bi-gcn: boundary-aware input-dependent graph convolution network for biomedical image segmentation. *arXiv preprint arXiv:2110.14775*, 2021.
- [46] Petar Veličković, Guillem Cucurull, Arantxa Casanova, Adriana Romero, Pietro Lio, and Yoshua Bengio. Graph attention networks. *arXiv preprint arXiv:1710.10903*, 2017.
- [47] Jiaxuan You, Rex Ying, and Jure Leskovec. Position-aware graph neural networks. In *International conference on machine learning*, pages 7134–7143. PMLR, 2019.

- [48] Sara Sabour, Nicholas Frosst, and Geoffrey E Hinton. Dynamic routing between capsules. *Advances in neural information processing systems*, 30, 2017.
- [49] Jaewoong Choi, Hyun Seo, Sui Im, and Myungjoo Kang. Attention routing between capsules. In *Proceedings of the IEEE/CVF International Conference on Computer Vision Workshops*, pages 0–0, 2019.
- [50] Zhang Xinyi and Lihui Chen. Capsule graph neural network. In *International conference on learning representations*, 2019.
- [51] Saurabh Verma and Zhi-Li Zhang. Graph capsule convolutional neural networks. *arXiv preprint arXiv:1805.08090*, 2018.
- [52] Rodney Lalonde, Naji Khosravan, and Ulas Bagci. Deformable capsules for object detection. *arXiv preprint arXiv:2104.05031*, 2021.
- [53] Geoffrey E Hinton, Sara Sabour, and Nicholas Frosst. Matrix capsules with em routing. In *International conference on learning representations*, 2018.
- [54] Vittorio Mazzia, Francesco Salvetti, and Marcello Chiaberge. Efficient-capsnet: Capsule network with self-attention routing. *Scientific reports*, 11(1):14634, 2021.
- [55] Rodney LaLonde, Ziyue Xu, Ismail Irmakci, Sanjay Jain, and Ulas Bagci. Capsules for biomedical image segmentation. *Medical image analysis*, 68:101889, 2021.

- [56] Yongping Du, Xiaozheng Zhao, Meng He, and Wenyang Guo. A novel capsule based hybrid neural network for sentiment classification. *IEEE Access*, 7:39321–39328, 2019.
- [57] Joes Staal, Michael D Abràmoff, Meindert Niemeijer, Max A Viergever, and Bram Van Ginneken. Ridge-based vessel segmentation in color images of the retina. *IEEE transactions on medical imaging*, 23(4):501–509, 2004.
- [58] AD Hoover, Valentina Kouznetsova, and Michael Goldbaum. Locating blood vessels in retinal images by piecewise threshold probing of a matched filter response. *IEEE Transactions on Medical imaging*, 19(3):203–210, 2000.
- [59] Renoh Johnson Chalakkal, Waleed H Abdulla, and S Sinumol. Comparative analysis of university of auckland diabetic retinopathy database. In *Proceedings of the 9th International Conference on Signal Processing Systems*, pages 235–239, 2017.
- [60] Cathie Sudlow, John Gallacher, Naomi Allen, Valerie Beral, Paul Burton, John Danesh, Paul Downey, Paul Elliott, Jane Green, Martin Landray, et al. Uk biobank: an open access resource for identifying the causes of a wide range of complex diseases of middle and old age. *PLoS medicine*, 12(3):e1001779, 2015.
- [61] Manuel Emilio Gegúndez-Arias, Arturo Aquino, José Manuel Bravo, and Diego Marín. A function for quality evaluation of retinal vessel

- segmentations. *IEEE transactions on medical imaging*, 31(2):231–239, 2011.
- [62] Zengqiang Yan, Xin Yang, and Kwang-Ting Cheng. A skeletal similarity metric for quality evaluation of retinal vessel segmentation. *IEEE transactions on medical imaging*, 37(4):1045–1057, 2017.
- [63] Khan Bahadar Khan, Muhammad Shahbaz Siddique, Muhammad Ahmad, and Manuel Mazzara. A hybrid unsupervised approach for retinal vessel segmentation. *BioMed Research International*, 2020, 2020.
- [64] Z. Yan, X. Yang and K. Cheng. A three-stage deep learning model for accurate retinal vessel segmentation. *IEEE journal of Biomedical and Health Informatics*, 23(4):1427–1436, 2018.
- [65] Xu Sun, Huihui Fang, Yehui Yang, Dongwei Zhu, Lei Wang, Junwei Liu, and Yanwu Xu. Robust retinal vessel segmentation from a data augmentation perspective. In *International Workshop on Ophthalmic Medical Image Analysis*, pages 189–198. Springer, 2021.
- [66] Xiang Li, Wenhai Wang, Xiaolin Hu, and Jian Yang. Selective kernel networks. In *Proceedings of the IEEE/CVF Conference on Computer Vision and Pattern Recognition*, pages 510–519, 2019.
- [67] Jie Hu, Li Shen, and Gang Sun. Squeeze-and-excitation networks. In *Proceedings of the IEEE conference on computer vision and pattern recognition*, pages 7132–7141, 2018.
- [68] Sanghyun Woo, Jongchan Park, Joon-Young Lee, and In So Kweon.

- Cbam: Convolutional block attention module. In Proceedings of the European conference on computer vision (ECCV), pages 3–19, 2018.
- [69] Huisi Wu, Jiasheng Liu, Wei Wang, Zhenkun Wen, and Jing Qin. Region-aware global context modeling for automatic nerve segmentation from ultrasound images. In Proceedings of the AAAI Conference on Artificial Intelligence, volume 35, pages 2907–2915, 2021.
- [70] Zekun Tong, Yuxuan Liang, Changsheng Sun, David S Rosenblum, and Andrew Lim. Directed graph convolutional network. arXiv preprint arXiv:2004.13970, 2020.